https://doi.org/10.1016/j.applthermaleng.2017.07.149

A detailed study on the effects of sunshape and incident angle on the optical performance of parabolic trough solar collectors

Bin Zou[1, 2,*], Hongxing Yang[1], Yang Yao[2] and Yiqiang Jiang[2]

[1] Renewable Energy Research Group (RERG), Department of Building Services Engineering, The Hong Kong Polytechnic University, Hong Kong, China

[2] Department of Building Thermal Energy Engineering, Harbin Institute of Technology, Harbin, China

Abstract

The influences of sunshape and incident angle on the optical performance of the parabolic trough solar collector (PTC) are investigated comprehensively based on Monte Carlo Ray Tracing (MCRT) method and theoretical analysis. This study adopts the acceptance-rejection sampling method, instead of the direct sampling method, for random variable sampling to reduce computing complexity. Both the energy proportion bounded by any angle span in the optical cone and the end loss caused by any incident angle are derived theoretically. It is revealed that the sunshape has great effects on the optical performance of a PTC, which should be taken into consideration in practice. The geometrical configuration of the PTC, especially the absorber tube

diameter, should be determined to meet the energy requirement based on local sunshape (circumsolar ratio) conditions. It is also found that the end loss, caused by the incident angle, weakens the optical efficiency. Larger aperture width and smaller absorber diameter will cause greater end loss for constant incident angle. When the absorber length is long enough, the effect of incident angle will be negligible. In a range of small focal lengths, the optical efficiency increases with the increase of focal length, and then decreases constantly with further increasing focal length. Findings in this paper can be used as reference or guidance for designing and optimizing PTC's structure in practice.

Keywords: Parabolic trough solar collector; Optical performance; Sunshape; Incident angle; Geometrical parameters.

* Corresponding author: Renewable Energy Research Group (RERG), Department of Building Services Engineering, The Hong Kong Polytechnic University, Hong Kong, China

E-mail address: zoubin9005@163.com (B. Zou)

Nomenclature

CL	local concentration ratio	θ_{in}	incident angle (°)
CL_i	local concentration ratio of the ith grid	θ_{inc}	radial intercepted angle (mrad)
d_a	absorber tube out diameter (m)	θ_s	radial angle of point on the sun (mrad)
d_g	glass envelope out diameter (m)	ρ_r	reflectivity of the parabolic reflector
$d_{\min}$	critical absorber tube diameter (m)	τ_g	transmissivity of the glass envelope
f	focal length (m)	φ_a	circumferential angle of the absorber (°)
I_D	direct normal solar radiation intensity (W/m^2)	φ_s	circumferential angle of the point on the sun (mrad)
I_{eff}	effective solar radiation intensity incident on the aperture (W/m^2)	χ	circumsolar ratio (CSR)
I_i	local energy flux density of the ith grid (W/m^2)	ψ_{rim}	rim angle (°)
L_a	absorber tube length (m)	κ_1~ κ_5	random number
$L_{end,\ loss}$	end loss (m)	***Abbreviations***	
W	aperture width (m)	ACR	active cavity radiometer
Greek symbols		CSP	concentrating solar power
α_a	absorptivity of the absorber	CSR	circumsolar ratio (χ)
δ	radial angle of the solar disk (δ =4.65mrad)	MCM	Monte Carlo Method
δ_Δ	radial angle of the circumsolar region (δ_Δ=43.6mrad)	MCRT	Monte Carlo Ray Tracing
η_o	optical efficiency (%)	RTM	Ray Tracing Method
θ	angular displacement of the line light source in the optical cone (°)	PTC	parabolic trough solar collector

1. Introduction

Solar energy has been exploited and utilized over years to meet the increasing energy demand, and to relieve the severe environmental issues [1-3]. Concentrating solar power (CSP) has developed into the most widely used form in solar thermal field [4, 5], among which parabolic trough solar power technology is the most cost-effective and developed one [6, 7]. Apart from power generation, parabolic trough solar collectors (PTCs) have also been used in many other areas, such as industrial process heat production, desalination, refrigeration and air-conditioning [8-11], showing promising development.

Parabolic trough solar collector (PTC), which is composed of a parabolic reflector and a receiver tube located at the focal line, is the most important component of a PTC system. The optical performance of the PTC is of great significance to the overall performance of the whole system. During 1970s and 1980s, Scholars [12-16] investigated the basic optical characteristics of the PTC, using optical cone method combined with integral method. Thomas et al. [17] investigated the effects of optical errors on flux distribution around the absorber. In their study, the occurrence of different optical errors was assumed to follow an independent stochastic process and presented by a normal distribution. Grena [18, 19] proposed a three-dimensional model and discussed the efficiency gain with an infrared-reflective film on the non-radiation part of the receiver. In recent years, with the development of computer technology, the Monte Carlo Ray Tracing (MCRT) method has been widely used to

study the optical properties of concentrating solar collectors due to its high accuracy and flexibility [20-22]. Cheng et al. [23-25] developed a unified MCRT code for simulating typical concentrating solar collectors and investigated the performance of different PTCs based on the self-developed code. Guo et al. [26] discussed the influences of various operational conditions in terms of both heat loss and exergy loss. They argued that optical heat loss far outweighed the heat loss of the receiver. Zou et al. [27] discussed the optical performance of the PTC comprehensively based on MCRT and theoretical analysis. Several critical parameters have been derived theoretically in their study and can be used to explain the simulation results very well. Zhang et al. [28] evaluated the effects of three kinds of geometrical deformations on the optical performance of the PTC and presented that the elliptic profile of the concentrator created a local hot spot on the absorber, which would shorten the absorber's service life.

Although numerous studies have been conducted on the optical performance of the PTC, few of them have taken into account the effects of actual sunshape and incident angle which are defined as the practical external conditions in this study. When propagating through the atmosphere, the solar beam interacts with atmospheric particles, which will cause small angle forward scattering, producing a solar aureole (circumsolar region) [29, 30]. Because of the limb darkening and atmospheric attenuation scattering, the radiant intensity distribution on the solar image obtained on the earth, defined as sunshape, is uneven and varies with the geographic locations [29,

31]. The practical sunshape has great effects on the optical performance of the PTC, which, however, has seldom been discussed in previous literature which always viewed the sunshape as a uniform model without considering the circumsolar region. To describe the actual solar energy profile precisely, Buie et al. [30] developed a generic sunshape model based on the vast data collected by the Lawrence Berkeley Laboratories (LBL) and the German Aerospace Center (DLR). In their later study [32], the effect of circumsolar region on the solar concentrating system was also investigated. However, it has not talked about the effects of sunshape for different geometrical parameters, and also not discussed the energy proportion for specific line light source span in the optical cone. In addition, the end loss which is caused by the incident angle weakens the optical efficiency obviously, especially for relatively short PTCs [33-36]. In this paper, the incident angle is defined as the angle between the incident rays and the cross-section of the PTC (XOY plane in Fig. 1). Xu et al. [35, 36] investigated the effects of end loss on the optical efficiency and talked about three end loss compensation strategies. However, they did not discuss the effects of end loss on the energy flux distribution on the absorber, and not study the optical performance for different geometrical parameters as well.

Unlike optical errors which are caused by the PTC system itself, sunshape and incident angle are usually determined by external conditions, such as location, time, atmospheric quality, installation direction. Therefore, the sunshape and incident angle can be viewed as practical external conditions in research. Based on coordinate

transformation and MCRT, the effects of those two practical factors on the optical performance are discussed comprehensively in this study. Unlike previous researches viewing the sunshape as a uniform solar disk, which used the direct sampling method for random variable sampling, this study adopts the acceptance-rejection sampling method instead, which will make the computing process more time-saving and efficient. The probability model of sunshape is established based on Buie's sunshape model [30]. In addition, both the energy proportion bounded by angular displacement of any line light source in the optical cone and the end loss against different geometrical parameters are derived theoretically. The effects of sunshape and incident angle on the optical performance for different geometrical configurations are investigated in detail.

2. Model and methodology description

2.1 PTC model

Fig. 1 shows the cross-sectional view of a parabolic trough solar collector (PTC)., It can be seen from the figure that a PTC module consists mainly of a parabolic trough reflector and a receiver tube that is composed of a metal absorber tube whose surface has been deposited absorbing coatings, and a glass envelope. Between the metal absorber and the glass envelope, there is a vacuum annulus to reduce heat loss and protect the coatings from oxidation. Some important parameters of the PTC, such as the aperture width (W), the focal length (f), the absorber tube outer diameter (d_a), the glass envelope diameter (d_g), the rim angle (ψ_{rim}), the radial angle of the solar

profile obtained on the earth ($\delta_{\triangle}$) and the circumferential angle of the absorber (φ_a), are also presented in the figure. A Cartesian coordinate system is established, the origin (O) of which is the vertex of parabola. The cross section of the parabolic trough is contained in X-Y plane, and Z axis is passing through the vertex and parallel to the focal line.

The present work is a further study on the optical performance of the PTC presented in Ref. [27]. Thus, the SEGS LS-2 PTC module which has be tested comprehensively at Sandia National Laboratory (SNL) [37] is also used as the physical prototype for study, the specifications of which are shown in Table 1.

2.2 Sunshape model

As mentioned above, limb darkening and atmospheric attenuation scattering cause non-uniform radiant intensity distribution, producing uneven sunshape. To describe the radial energy profile (i.e. sunshape) precisely, Buie et al. [30] developed a generic solar model based on the vast data collected by the Lawrence Berkeley Laboratories (LBL) and the German Aerospace Center (DLR). In Buie's model, the brightness at any point was normalized against the central intensity. The expression of the model is given by Eq. (1).

$$\phi(\theta_s)=\begin{cases}\dfrac{\cos(0.326\theta_s)}{\cos(0.308\theta_s)} & \theta_s \le 4.65mrad \\ e^{\kappa}\theta_s^{\gamma} & \theta_s > 4.65mrad\end{cases} \tag{1}$$

where θ_s is the radial angular displacement (radial angle) of any point on the sun, κ and γ are given by Eq. (2) and Eq. (3) respectively.

$$\kappa = 0.9\ln(13.5\chi)\chi^{-0.3} \tag{2}$$

$$\gamma = 2.2\ln(0.52\chi)\chi^{0.43} - 0.1 \tag{3}$$

where χ is the circumsolar ratio (i.e. CSR), which is defined as the ratio of the energy contained within the circumsolar region (aureole) to the total energy contained in both the solar disk and aureole, and given by Eq. (4).

$$\chi = \frac{2\pi\int_{\delta}^{\delta_\Delta}\phi(\theta)\sin(\theta)d\theta}{2\pi\int_{0}^{\delta_\Delta}\phi(\theta)\sin(\theta)d\theta} \tag{4}$$

where δ and δ_Δ are the radial angular size of the solar disk (δ =4.65mrad) and the circumsolar region respectively.

From Eq. (1) ~ Eq. (4), it can be seen that the circumsolar ratio (CSR) is a very important parameter determining the sunshape, which is correlated with geographic locations and atmospheric conditions. The CSR can be practically measured by a pyrheliometer or active cavity radiometer (ACR) [29, 30]. Different pyrheliometers or ACRs have different acceptance angles (usually ranging between 5° and 7°). In Buie's study [30], the acceptance angle was determined as 5° in order to keep consistent with the database of LBL. Hence, in this study, 5° or alternatively expressed as the radial angular displacement of 2.5° (43.6mrad) is also used as the upper limit of the circumsolar region (i.e. δ_Δ =43.6mrad). As a matter of fact, by summarizing and analyzing the meteorological parameters, the average or dominant CSR which is usually used as the representative CSR for a specific site can be easily obtained. It was proved that it is a linear relationship between the radiation profile (sunshape) and the radial angle in the circumsolar region in log-log space [30], which is shown in

Fig.2.

2.3 MCRT model

Monte Carlo Ray Tracing (MCRT) method which has great flexibility and accuracy, is a powerful tool for simulating the optical performance of the PTC. It combines the Monte Carlo Method (MCM) with the Ray Tracing Method (RTM). Detailed information about MCRT can be referred in Ref. [27].

Simulation conducted in this paper is based on two assumptions: (1) The reflectivity, transmissivity and absorptivity are independent of the incident angle. (2) The effects of the refraction of glass envelope and the reflection of absorber tube are ignored. This study will discuss the optical performance of PTCs under conditions of non-zero incident angle. To be more general, the non-zero incident angle model is presented, the schematic of which is shown in Fig. 3.

As Fig. 3 depicts, two Cartesian coordinate systems (OXYZ and O'X'Y'Z') are established. The coordinate of hitting point (x_0, y_0, z_0) in coordinate system OXYZ can be expressed by Eq. (5).

$$\begin{cases} x_0 = W \cdot \kappa_1 - W/2 \\ y_0 = x_0^2 / 4f \\ z_0 = L_a \cdot \kappa_2 \end{cases} \tag{5}$$

The unit direction vector of the incident ray in coordinate system O'X'Y'Z' is given by Eq. (6).

$$\overrightarrow{S'} = \left(\sin\theta_s \cos\varphi_s,\ -\cos\theta_s,\ \sin\theta_s \sin\varphi_s\right) \tag{6}$$

The unit direction vector ($\overrightarrow{S'}$) in coordinate O'X'Y'Z' has to be transformed to

the vector ($\vec{S}$) in coordinate system OXYZ. As Fig. 3 shows, the coordinate O'X'Y'Z' is realized through translation and rotation of coordinate OXYZ. Given that the translation does not change a vector, only the effect of rotation needs to be considered. The schematic of coordinate transformation for the incident ray vector between O'X'Y'Z' and OXYZ is shown in Fig. 4. From the figure, for any point P, the following geometrical relations can be easily obtained.

$$\begin{cases} x_{\mathrm{p}} = x_{\mathrm{P}}' \\ y = \mathrm{OE} = \mathrm{AP} = \mathrm{AD} + \mathrm{DP} = \mathrm{BC} + \mathrm{DP} = \mathrm{OC} \cdot \sin\theta_{in} + \mathrm{PC} \cdot \cos\theta_{in} = z_{\mathrm{P}}' \cdot \sin\theta_{in} + y_{\mathrm{P}}' \cdot \cos\theta_{in} \\ z = \mathrm{OA} = \mathrm{OB} - \mathrm{AB} = \mathrm{OB} - \mathrm{CD} = \mathrm{OC} \cdot \cos\theta_{in} - \mathrm{PC} \cdot \sin\theta_{in} = z_{\mathrm{P}}' \cdot \cos\theta_{in} - y_{\mathrm{P}}' \cdot \sin\theta_{in} \end{cases} \quad (7)$$

Thus, the coordinate transformation matrix (M) from O'X'Y'Z' to OXYZ can be expressed as Eq. (8).

$$\mathrm{M} = \begin{bmatrix} 1 & 0 & 0 \\ 0 & \cos\theta_{in} & \sin\theta_{in} \\ 0 & -\sin\theta_{in} & \cos\theta_{in} \end{bmatrix} \quad (8)$$

Therefore, the unit direction vector ($\vec{S}$) in coordinate system OXYZ can be given by Eq. (9)

$$\vec{S} = \mathrm{M} \cdot \vec{S}' \quad (9)$$

Easily, the inner normal unit vector of the parabolic reflector and the glass envelope can be derived and given by Eq. (10) and Eq. (11), respectively.

$$\vec{n_0} = \left(-x / \sqrt{x^2 + 4f^2},\ \ 2f / \sqrt{x^2 + 4f^2},\ \ 0 \right) \quad (10)$$

$$\vec{n_1} = \left(-2x / d_g,\ \ -2(y - f) / d_g,\ \ 0 \right) \quad (11)$$

According to Fresnel law, the following equation can be obtained for $\vec{\lambda}$, $\vec{n}$ and $\vec{r}$ representing the unit incident vector, the normal unit vector, and the unit reflected

vector of a surface (parabolic reflector or glass cover) respectively.

$$\vec{r} = \vec{\lambda} - 2 \cdot (\vec{\lambda} \cdot \vec{n}) \cdot \vec{n} \tag{12}$$

The optical behavior (reflection, absorption or transmission) on a surface is determined depending on a uniformly generated random number. For example, a uniformly generated random number (κ_3) will be used to compare with the reflectivity (ρ_r) of the reflector when a ray reaches the surface of the reflector. If $\kappa_3 \le \rho_r$, the ray is reflected, or it will be abandoned. Other optical behaviors, including transmission and reflection of the glass cover and absorption of the absorber tube, are determined by the same way. For clarity, the flowchart of MCRT is shown in Fig. 5.

To initialize the position of the ray on the sun, the probability distribution function is required, which can be derived using the sunshape model and given by Eq. (13).

$$F(x) = \frac{\int_0^x \phi(\theta)\sin(\theta)d\theta}{\int_0^{\delta_\Delta} \phi(\theta)\sin(\theta)d\theta} \tag{13}$$

Therefore, its probability density function can be given by Eq. (14).

$$f(x) = \frac{\phi(x)\sin(x)}{\int_0^{\delta_\Delta} \phi(\theta)\sin(\theta)d\theta} \tag{14}$$

From Eq. (1) and Eq. (13), we can see that it is very difficult to find directly the inverse function for Eq. (13). Thus, the direct sampling method may be not applicable in this study. Instead, we use the acceptance-rejection sampling method (or hit-and-miss method) for random variable sampling, the principle of which is

expounded as follows:

The distribution density function $f(x)$ is defined between a and b ($a \le x \le b$), and M is the upper limit of $f(x)$ (i.e. $0 < f(x) \le M$). Two uniformly distributed random numbers κ_4 and κ_5 are generated. If $M\kappa_5 \le f\left(a+(b-a)\kappa_4\right)$, accept κ_4, otherwise abandon κ_4. The flowchart of the acceptance-rejection sampling method is shown in Fig. 6.

3. Parameter derivation and definition

The reflection process of sun rays is shown in Fig. 7, from which we can see that the sun can be viewed as consisting of countless line light sources that are parallel to the axial direction (Z-axis) of the absorber. It is easily understood that the line light sources on the sun will also form line lights on the absorber surface after reflection (as shown in Fig. 7). The intensity of any line light source in the optical cone with a unit height can be derived theoretically based on aforementioned sunshape model, and given by Eq. (15).

$$\psi(\theta) = 2 \times \int_0^{\sqrt{\delta_\Delta{}^2 - \theta^2}} \phi\left(\sqrt{\theta^2 + \tau'^2}\right) d\tau' \tag{15}$$

where θ is the radial angular displacement of line light source. Therefore, the total energy in any angle span ($\Delta\theta$) in the light cone can be calculated by Eq. (16).

$$\Phi(\Delta\theta) = \int_{\Delta\theta} \psi(\theta) d\theta \tag{16}$$

Consequently, the proportion of the energy bounded by a specific radial angular displacement (θ) of a certain line light source can be given by Eq. (17).

$$P(\theta)=\frac{2\times\int_0^{\theta}\psi(\tau)d\tau}{2\times\int_0^{\delta_\Delta}\psi(\tau)d\tau} \tag{17}$$

As Fig. 8 shows, partial reflected rays in the light cone are intercepted by the absorber tube. Obviously, the radial intercept angle (θ_{inc}) of the absorber for any point A on the reflector can be given by Eq. (18).

$$\theta_{inc}=\arcsin\left[d_a/\left(2\times\sqrt{x_{\mathrm{A}}^2+(x_{\mathrm{A}}^2/4f-f)^2}\right)\right] \tag{18}$$

The critical tube diameter ($d_{\min}$) is defined as the required minimum outer diameter of the absorber to avoid rays escaping, which can be expressed by Eq. (19) [24, 27].

$$d_{\min}=2\cdot\left(W^2/16f+f\right)\cdot\sin\delta_\Delta \tag{19}$$

As shown in Fig. 3, partial reflected rays cannot reach the absorber due to the incident angle (θ_{in}), causing end loss $L_{end,loss}$ [35, 36]. The centrally reflected ray from an arbitrary point A (O') on the reflector intersects with the focal line at point F. HF is the end loss ($L_{end,loss}$) corresponding to point A. In △AHF, the length of HF can be calculated by Eq. (20).

$$\Delta z=z_{\mathrm{F}}-z_{\mathrm{A}}=\mathrm{HF}=\mathrm{AH}\cdot\tan\theta_{in}=\left(x_{\mathrm{A}}^2/4f+f\right)\cdot\tan\theta_{in} \tag{20}$$

Due to the incident angle (θ_{in}), the effective solar radiation intensity (I_{eff}) incident on the aperture should be calculated by Eq. (21).

$$I_{eff}=I_D\cos\theta_{in} \tag{21}$$

The local concentration ratio (CL_i) is defined as the ratio of local energy flux density (I_i) to the effective solar radiation intensity (I_{eff}) incident on the aperture [24],

and expressed by Eq. (22).

$$CL_i = I_i / I_{eff} \tag{22}$$

4. Model validation

4.1 Suitable grid configuration and number of rays

In our previous study [27], 180 grid divisions around the absorber were proved to be appropriate, and hence also be adopted in present work. When the incident angle (θ_{in}) is not zero, the energy flux density distribution along the length (Z-axis) direction is also uneven. Thus, the absorber should also be divided into a certain number of small sections along the length direction. Given that the length of the used PTC module is not very long (L_a=7.8 m), 30 sections are divided along the length direction of the absorber.

The number of rays should be determined considering both the results' accuracy and the computing time. In Refs. [24, 25], 5×10^7 rays were proved to be large enough to obtain accurate results. However, in those two references, the incident angle was always kept zero, and the absorber was regarded as a whole along the length direction. In this paper, the effects of incident angle (θ_{in}) will be discussed, and the absorber is divided into many small sections along the length direction, which may need more number of rays to match. In current work, 1×10^8 rays are adopted for the simulation.

4.2 Model validation

Fig. 9 shows the distribution of the local concentration ratio (*CL*) obtained by the established models and Jeter's results [15]. As Fig. 9 presents, the two curves agree

very well with each other, verifying the accuracy of the established optical models. It is also clearly seen that the distribution of local concentration ratio (*CL*) can be divided into four parts [24,25, 27], which are the shelter region (part Ⅰ), the energy flux increasing region (part Ⅱ), the energy flux decreasing region (part Ⅲ) and the direct insolation region (part Ⅳ) respectively.

5. Results and discussion

As mentioned above, the SEGS LS-2 PTC module, parameters of which are given in Table 1, is used as the physical prototype for this study. The direct normal solar radiation intensity (I_D) is 1000W /m^2. The effects of sunshape and incident angle on the optical performance of the PTC will be discussed and the findings will be expounded in depth in the next section.

5.1 Effects of sunshape

Fig. 10 shows the effects of circumsolar ratio (CSR) on the optical efficiency (η_o). It can be seen from the figure that η_o decreases obviously with the increase of CSR. When the CSR increases from 0 to 0.5, the optical efficiency decreases from 84.85% to 77.42%, dropping by 7.43%. Using Eq. (19), we can obtain the minimum radial intercept angle ($\theta_{inc,\min}$) for the LS-2 PTC module, the value of which is 17.05mrad. Obviously, the minimum radial intercept angle ($\theta_{inc,\min}$) is less than the upper limit of the radial angular displacement of the sun (δ_Δ =43.6mrad), causing rays escaping and hence weakening the optical efficiency. With the increase of CSR, the proportion of the energy escaping from the PTC increases, leading to greater optical

loss and thus causing decrease of optical efficiency. From the analysis above, we can see that the effects of the sunshape on the optical performance of a PTC is remarkable, which should be taken into consideration in practice. It is necessary for us to collect and summarize the dominant sunshape (CSR) when studying the performance of a PTC system for a specific geographic location. Fig. 11 depicts the effects of circumsolar ratio (CSR) on the distribution of local concentration ratio (*CL*). From the figure, we can see that the maximum *CL* decreases and the sum of the angle span for part Ⅰ, part Ⅱ, and part Ⅲ increases with the increase of CSR, indicating a more uniform distribution of energy flux on the absorber surface. It also shows that when the CSR increases to a certain value (about 0.8), part Ⅰ and part Ⅱ will disappear.

Fig. 12 shows the variation of optical efficiency (η_o) with absorber diameter (d_a) for different circumsolar ratio (CSR). It is obviously seen that η_o increases consistently with the increase of d_a for CSR more than zero. This is because the larger the diameter (d_a) is, the larger the radial intercept angle (θ_{inc}) will be, thus receiving more reflected rays. From the figure, we can also find that when CSR is equal to zero (CSR=0), η_o increases firstly for d_a less than 25mm, and then maintains almost constant at the maximum (about 84.85%) with the increase of d_a. This can be easily explained by the critical diameter given by Eq. (20). When CSR=0, all the rays come from the solar disk (without aureole) the radial angle of which is 4.65mrad (δ=4.65mrad). Using Eq. (20), we can calculate the critical diameter for δ, the value of which is 25mm ($d_{\min}$=25mm). Consequently, when d_a is smaller than

$d_{\min}$, partial reflected rays will escape from around the absorber tube (escaping effect), reducing optical efficiency (η_o), and when d_a is larger than $d_{\min}$, all the rays will be received by the absorber, ensuring the maximum optical efficiency. We can also see from the figure that the larger the CSR is, the smaller η_o will be, which shows the same characteristics that is shown in Fig. 10. The optical efficiency difference between two CSRs decreases with the increase of absorber diameter (d_a), which indicates that the optical efficiency will be less sensitive to the CSR for a PTC with larger absorber diameter.

Fig. 13 shows the effects of the aperture width (W) on the optical efficiency (η_o) for CSR=0.4. It can be obviously seen that η_o increases constantly from 81.16% to 71.32% with increasing W from 1m to 16m. The possible reason is displayed in Fig. 14 which shows the variation of the radial intercept angle (θ_{inc}) with the absolute value of the abscissa of point A ($|x_A|$). It can be clearly observed from Fig. 14 that θ_{inc} deceases consistently with the increase of $|x_A|$, which means that the larger W is, the smaller θ_{inc} will be, causing greater rays escaping and thus lowering optical efficiency (η_o). Therefore, a larger absorber diameter will be required for the PTC with larger aperture width to acquire a relatively high optical efficiency. The effects of focal length (f) on optical efficiency (η_o) for CSR=0.4 is shown in Fig. 15, from which we can find that η_o increases firstly and after getting to the peak (about 82.4%) at f=0.8, η_o decreases constantly with further increasing f. The reason is shown in Fig. 16 which depicts the variation of the radial intercept angle (θ_{inc}) with

focal length (f) for different reflection point A ($|x_A|$). It is clearly seen from the figure that when $|x_A|$ is more than 1, θ_{inc} increases firstly and then deceases with the increase of f, showing similar variation trend to η_o which is depicted in Fig. 15. Fig. 16 also shows that the focal length (defined as f_p) corresponding to the peak efficiency increases with the increase of $|x_A|$. As a result, the f_p for a specific PTC will be determined by the combined effects of all the reflection points on the parabolic reflector. It can be inferred from the analysis above that the larger W is, the larger f_p will be.

For more generalization, the energy proportion (P) bounded by radial angular displacement (θ) of line light source in the optical cone for different CSR is shown in Fig. 17. Obviously, the energy proportion (P) increases with the increase of θ. As CSR increases, P decreases for a specific θ, which means the larger CSR is, the larger the absorber diameter (d_a) has to be to meet the energy requirement. For example, if it is acceptable for a site with a CSR of 0.3 to have 90% of the incoming total energy received by the absorber, the radial angular displacement (θ) should be more than 9mrad.

5.2 Effects of incident angle

As shown in Fig. 3, partial reflected rays will escape from one end of the PTC because of the incident angle (θ_{in}), causing end loss ($L_{end,loss}$), which will undoubtedly weaken the optical efficiency. The details of the effects of the incident angle (θ_{in}) on the optical performance of the PTC are discussed in this section. The

circumsolar ratio in this part is determined as zero (CSR=0). The length of the absorber (L_a) for the used PTC in this paper is 7.8 m (shown in Table 1). Fig. 18 shows the variation of optical efficiency (η_o) with the incident angle (θ_{in}). It can be clearly seen from the figure that η_o decreases obviously with the increase of θ_{in}. When θ_{in} is greater than 77°, η_o maintains constant at an extremely small value (almost zero). That means all the reflected beam escape from the PTC with θ larger than 77°. Fig. 19(a) and Fig. 19(b) show the distribution of local concentration ratio (*CL*) around and along the absorber respectively. Note that Fig. 19(b) shows the results for θ_{in}=30°. From Fig. 19(a), we can see that the sum of angle span for part Ⅰ, part Ⅱ, and part Ⅲ increases with the increase of θ_{in}. This is because the larger θ_{in} is, the greater the distance of the reflected rays from the reflector to the absorber (i.e. AF in Fig. 3) is, and thus the larger the solar image on the surface of the absorber will be. In addition, the peak value of *CL* decreases with the increase of θ_{in} and the energy flux distribution is consequently more uniform. It also shows that when the incident angle is more than 45°, part Ⅱ disappears. It can be observed in Fig. 19(b) that there is a section at one end of the absorber that has extremely small *CL* (almost zero), and afterwards, *CL* increases sharply to a relatively constant value as the absolute value of circumferential angle ($|\varphi_a|$) is smaller than 90°. When $|\varphi_a|$ is larger than 90°, the *CL* along the absorber is kept very small (almost zero), which means that all the reflected beam cannot reach the area where $|\varphi_a|$ is larger than 90°. It can also be found that when two circumferential angles are symmetrical to each

other (±45° and ±75° shown in Fig. 19(b)), the distributions of *CL* for them are coincident. From Fig. 19, we can also find that the length of the section with very low *CL* for $\varphi_a = \pm 75^{\circ}$ is larger than that for $\varphi_a = 0^{\circ}$ and $\varphi_a = \pm 45^{\circ}$. This can be explained by the theoretical results shown in Fig. 20, which depicts the variation of $z_{\mathrm{F}} - z_{\mathrm{A}}$ with $|x_{\mathrm{A}}|$ for different θ_{in}. From the figure, we can see that $z_{\mathrm{F}} - z_{\mathrm{A}}$ increases with the increase of $|x_{\mathrm{A}}|$, indicating that the wider the aperture width (*W*) is, the greater the end loss ($L_{end,loss}$) will be. The position with larger $|\varphi_a|$ can only receive the reflected rays from larger $|x_{\mathrm{A}}|$, leading to larger $z_{\mathrm{F}} - z_{\mathrm{A}}$. Therefore, the length of the section with very low *CL* for larger $|\varphi_a|$ will be greater than that for smaller $|\varphi_a|$. It can also be seen from Fig. 20 that when the incident angle (θ_{in}) is 77°, the minimum of $z_{\mathrm{F}} - z_{\mathrm{A}}$ is larger than L_a (L_a=7.8 m), which means that all the reflected beam escape from the PTC. This nicely explains the phenomenon shown in Fig. 18 that the optical efficiency (η_o) is almost zero for incident angle (θ_{in}) more than 77°, further verifying the accuracy and reliability of established optical models.

Figs. 21-24 show the effects of aperture width (W), focal length (f), absorber diameter (d_a) and absorber length (L_a) on the optical efficiency (η_o) respectively under the condition of θ_{in}=30°. From Fig. 21, we can see that η_o decreases continuously with the increase of W, which has be accounted for by the theoretical results presented in Fig. 20. Fig. 22 shows that η_o increases while f is less than 0.75 m, and then decreases constantly with further increasing f. The possible reason can be found in Fig. 25 which shows the effects of f on $z_{\mathrm{F}} - z_{\mathrm{A}}$ for

different $|x_A|$. From the figure, we can clearly see that when f is less than 0.75m, $z_F - z_A$ decreases with increasing f for $|x_A|$ larger than 1.75. This indicates that when f is smaller than 0.75 m, the end loss ($L_{end,loss}$) will decrease with increasing f for most $|x_A|$. Note that the maximum of $|x_A|$ is half the aperture width ($|x_A|_{max} = 0.5W = 2.5\text{m}$). Thus, a small increase of η_o occurs for f varying from 0 to 0.75m. Comparing Fig. 21 and Fig. 22, we can find that η_o decreases from 73.54% to 54.38% for *W* varying from 1 m to 16 m, dropping by 18.1%, and decreases from 75.38% to 10.73% for f varying from 0.5 m to 10.5 m, dropping by 64.65%, which indicates that η_o is more sensitive to *f* than to *W* for a certain incident angle (θ_{in}). It can be seen from Fig. 23 that when d_a is larger than 30mm, η_o increases gradually from 71.51% to 71.98% with d_a increasing from 30mm to 120mm. This because the larger d_a is, the more the incident rays will be absorbed directly and the less the rays can escape from around it. Whereas when d_a is less than 30 mm, η_o increases rapidly from 67.5% to 71.51% with d_a increasing from 20mm to 30mm. The possible reason is that the absorber diameter (d_a) is less than the critical diameter (d_{min}=30mm) in this case, causing serious rays escaping effect. From the discussion in section 5.1, we know that the critical diameter for θ_{in}=0° is 25mm. Therefore, it can be inferred that larger incident angle (θ_{in}) will cause larger critical absorber diameter (d_{min}), which will lead to larger rays escaping. Fig. 24 illustrates the effects of absorber length (L_a) on the optical efficiency (η_o) for θ_{in} =30°. From the figure, we can clearly see that η_o first increases rapidly from 64.38%

to 81.44% for L_a increasing from 5m to 30m, and then the growth rate becomes slower with further increasing L_a. When L_a is larger than 70 m, η_o maintains at a relatively high value of about 83%. This demonstrates that the longer L_a is, the smaller the effect of θ_{in} on η_o will be, and when L_a is larger than a certain degree, the effect of θ_{in} will be negligible.

6. Conclusions

The influences of actual sunshape and incident angle on the optical performance of the PTC is investigated comprehensively in this paper. Based on randomized trial theory and coordinate transformation, MCRT optical models are established. The energy proportion bounded by any angle span in the optical cone and the end loss caused by any incident angle are derived theoretically. Considering different sunshapes and incident angles, the effects of geometrical parameters on optical performance are discussed in detail. Compared with the results presented in related literature, the established optical models are validated. In addition, all the findings can also be explained by theoretical analysis results, further proving the accuracy and reliability of the established models. Findings in this paper can be used as reference or guidance for designing and optimizing PTC's structure in practice. Several conclusions are drawn as follows.

(1) The sunshape (represented by CSR) has great effects on the optical performance of a PTC, which should be taken into account in practice. The optical efficiency decreases obviously with increasing CSR. The distribution of energy flux

around the absorber tube is more uniform for larger CSR. The optical efficiency increases with increasing absorber diameter and decreases with increasing aperture width. The focal length corresponding to the peak efficiency increases with the aperture width. The energy proportion bounded by a certain angle span decreases with increasing CSR. In practice, the geometrical configuration of the PTC, especially the absorber tube diameter, should be appropriate to meet the energy requirement based on local CSR conditions.

(2) The end loss caused by incident angle weakens the optical efficiency. The larger the incident angle is, the greater the end loss will be, causing lower optical efficiency. Larger incident angle can improve the uniformity of the energy flux distribution around the absorber tube. The effects of the incident angle on the optical efficiency are closely associated with geometrical parameters. For any incident angle, larger aperture width, smaller absorber diameter and smaller absorber length cause greater end loss. When the absorber length is larger than a certain degree, the effect of incident angle will be negligible. When the focal length is in a range of certain small values, the optical efficiency increases with the increase of focal length, and then decreases constantly with further increasing focal length.

This paper has discussed the effects of external environmental factors (sunshape and incident angle) on the optical efficiency. In practice, optical errors, caused by the PTC system itself, also affect greatly the optical performance. Thus, the coupled effects of optical errors (tracking error, installation error and surface error) are also

very important, which are studied currently and will be presented in another paper.

Acknowledgements

The authors appreciate the financial support from the Hong Kong Housing Authority research project for the Joint Supervision Scheme (Grant No.: K-ZJHE).

References

[1] D. Vijay, A. Mansoor, S.S. Soma, et al. Solar energy: Trends and enabling technologies, Renewable and Sustainable Energy Reviews 19 (2013) 55-564.

[2] M. Raisul Islam, K. Sumathy, U.K. Samee, Solar water heating systems and their market trends, Renewable and Sustainable Energy Reviews 17 (2013) 1-25.

[3] Z.Y. Wang, W.S. Yang, F. Qiu, et al. Solar water heating: From theory, application, marketing and research, Renewable and Sustainable Energy Reviews 41 (2015) 68-84.

[4] X.H. Xu, K. Vignarooban, B. Xu, K. Hsu, et al. Prospects and problems of concentrating solar power technologies for power generation in the desert regions, Renewable and Sustainable Energy Reviews 53 (2016) 1106-1131.

[5] S.A. Kalogirou, Solar thermal collectors and applications, Progress in Energy and Combustion Science 30 (2004) 231-295.

[6] H. Price, E. Lupfert, D. Kearney, E. Zarza, et al. Advances in parabolic trough solar power technology, Journal of Solar Energy Engineering 124 (2002) 109-125.

[7] G.A. Fernandez, E. Zarza, L. Valenzuela, M. Perez, Parabolic-trough solar collectors and their applications, Renewable and Sustainable Energy Reviews 14

(2010) 1695-1721.

[8] S.A. Kalogirou, Parabolic trough collectors for industrial process heat in Cyprus, Energy 27 (2002) 813-830.

[9] A. Scrivani, T.E. Asmar, U. Bardi, Solar trough concentration for fresh water production and waste treatment, Desalination 206 (2007) 485-493.

[10] P. Bermejo, F.J. Pino, F. Rosa, Solar absorption cooling plant in Seville, Solar Energy 84 (2010) 1503-1512.

[11] F.J. Cabrera, A. Fernandez-Garcia, R.M.P. Silva, M. Perez-Garcia, Use of parabolic trough solar collectors for solar refrigeration and air-conditioning applications, Renewable and Sustainable Energy Reviews 20 (2013) 103-118.

[12] D.L. Evans, On the performance of cylindrical parabolic solar concentrators with flat absorbers, Solar Energy 19 (1977) 379-385.

[13] R.O. Nicolas, J.C. Duran, Generalization of the two-dimensional optical analysis of cylindrical concentrators, Solar Energy 25 (1980) 21-31.

[14] J.C. Duran, R.O. Nicolas, Development and application of a two-dimensional optical analysis of non-perfect cylindrical concentrators, Solar Energy 34 (1984) 257-269.

[15] S.M. Jeter, Calculation of the concentrated flux density distribution in parabolic trough collectors by a semifinite formulation, Solar Energy 37 (1986) 335-345.

[16] S.M. Jeter, The distribution of concentrated solar radiation in paraboloid collectors, Journal of Solar Energy Engineering 108 (1986) 219-225.

[17] A. Thomas, H.M. Guven, Effect of optical errors on flux distribution around the absorber tube of a parabolic trough concentrator, Energy Conversion and Management 35 (1994) 575-582.

[18] R. Grena, Optical simulation of a parabolic solar trough collector, International Journal of Sustainable Energy 29 (2010) 19-36.

[19] R. Grena, Efficiency Gain of a solar trough collector due to an ir-reflective film on the non-irradiated part of the receiver, International Journal of Green Energy 8 (2011) 715-733.

[20] Z.D. Cheng, Y.L. He, F.Q. Cui, R.J. Xu, et al. Numerical simulation of a parabolic trough solar collector with nonuniform solar flux conditions by coupling FVM and MCRT method, Solar Energy86 (2012) 1770-1784.

[21] A.A. Hachicha, I. Rodríguez, R. Capdevila, A. Oliva, Heat transfer analysis and numerical simulation of a parabolic trough solar collector, Applied Energy 111 (2013) 581-592.

[22] Z.D. Cheng, Y.L. He, F.Q. Cui, A new modelling method and unified code with MCRT for concentrating solar collectors and its applications, Applied Energy 101 (2013) 686-698.

[23] Z.D. Cheng , Y.L. He, F.Q. Cui, A new modelling method and unified code with MCRT for concentrating solar collectors and its applications. Applied Energy 101 (2013) 686-698.

[24] Z.D. Cheng Y.L., He, K. Wang, B.C. Du, et al. A detailed parameter study on the

comprehensive characteristics and performance of a parabolic trough solar collector system. Applied Thermal Engineering 63 (2014) 278-289.

[25] Z.D. Cheng, Y.L. He, F.Q. Cui, B.C. Du, et al. Comparative and sensitive analysis for parabolic trough solar collectors with a detailed Monte Carlo Ray-Tracing optical model, Applied Energy 115 (2014) 559-572.

[26] J.F. Guo, X.L. Huai, Z.G. Liu. Performance investigation of parabolic trough solar receiver, Applied Thermal Engineering 95 (2016) 357-364.

[27] B. Zou, J.K. Dong, Y. Yao, Y.Q. Jiang, A detailed study on the optical performance of parabolic trough solar collectors with Monte Carlo Ray Tracing method based on theoretical analysis, Solar Energy 147 (2017) 189-201.

[28] C.Z. Zhang, G.Q. Xu, Y.K. Quan, H.W. Li, et al. Optical sensitivity analysis of geometrical deformation on the parabolic trough solar collector with Monte Carlo Ray-Trace method, Applied Thermal Engineering 109 (2016) 130-137.

[29] A. Neumann, M. Schubnell, Irradiance and sunshape measurements for the Cologne site. In: Proceedings of the 8th International Solar Forum, 1992, pp. 1173-1183.

[30] D. Buie, A.G. Monger, C.J. Dey, Sunshape distributions for terrestrial solar simulations, Solar Energy 74 (2003) 113-122.

[31] A. Neumann, A. Witzke, S.A. Jones, G. Schmitt, Representative terrestrial solar brightness profiles, Journal of Solar Energy Engineering 124 (2002) 198-204.

[32] D. Buie, A.G. Monger, The effect of circumsolar radiation on a solar

concentrating system, Solar Energy 76 (2004) 181-185.

[33] M.M. EL-Kassaby, Prediction of optimum tilt angle for parabolic trough with the long axis in the north-south direction, International Journal of Solar Energy 16 (1994) 99-109.

[34] A.S. Hegazy, M.M. El-Kassaby, M.A. Hassab Effect of parabolic trough solar collector orientation on its collection efficiency, International Journal of Solar Energy 16 (1995) 173-183.

[35] C.M. Xu, Z.P. Chen, M. Li, P. Zhang, et al. Research on the compensation of the end loss effect for parabolic trough solar collectors, Applied Energy 115 (2014) 128-139.

[36] M. Li, C.M. Xu, X. Ji, P. Zhang, et al. A new study on the end loss effect for parabolic trough solar collectors, Energy 82 (2015) 382-394.

[37] V. Dudley, G. Kolb, M. Sloan, D. Kearney, SEGS LS2 solar collector–test results, Report of Sandia National Laboratories, 1994, SANDIA 94-1884, USA.

Figures:

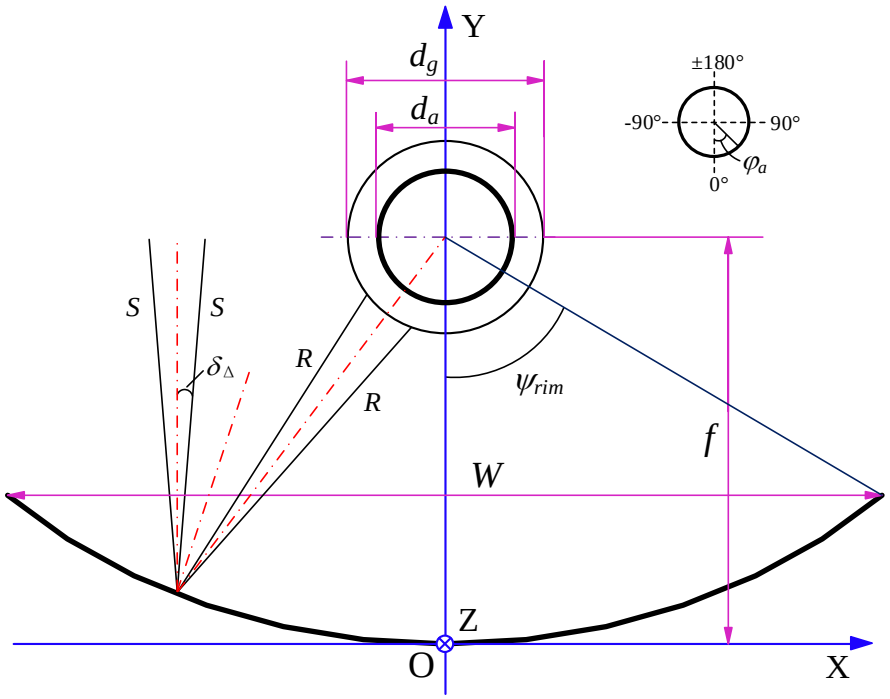

Fig. 1 Schematic diagram of the cross section of a PTC module

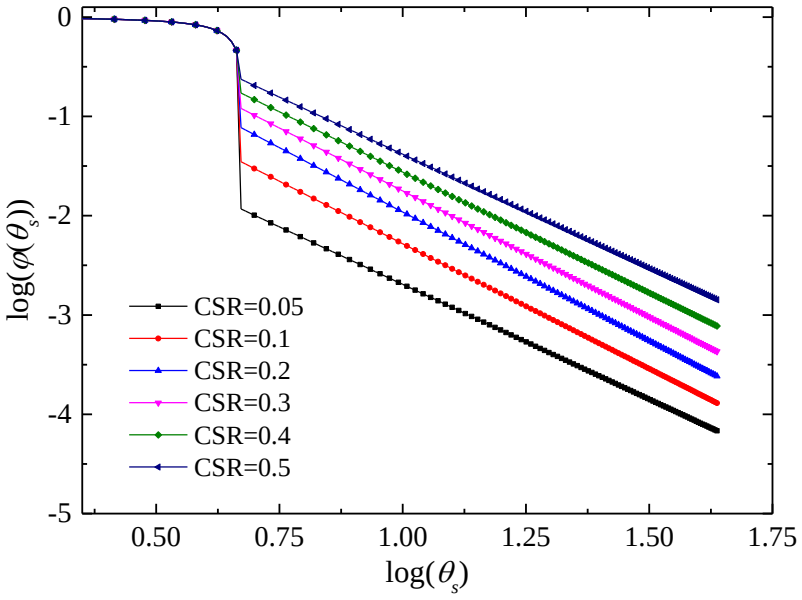

Fig. 2 Sunshape described by Buie's model for different CSR

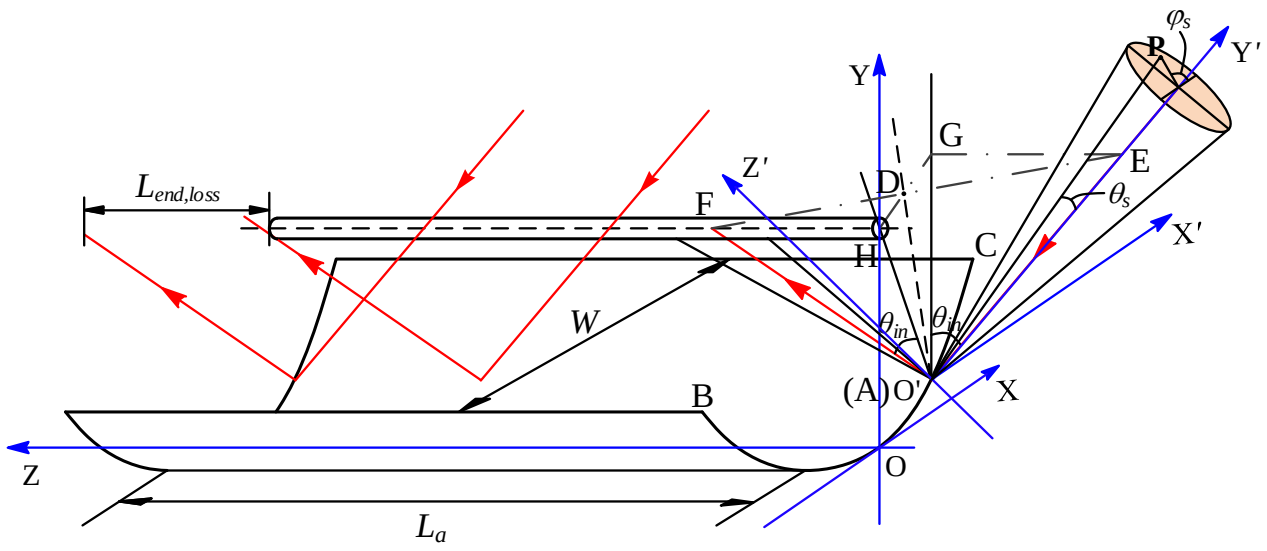

Fig. 3 Schematic of rays concentration for a PTC with non-zero incident angle

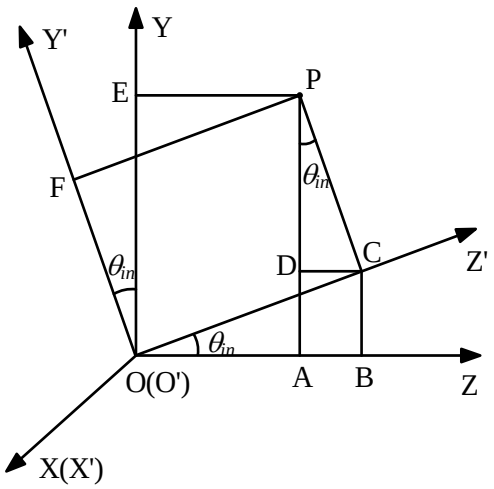

Fig. 4 Coordinate transformation for the incident ray vector between O'X'Y'Z' and OXYZ

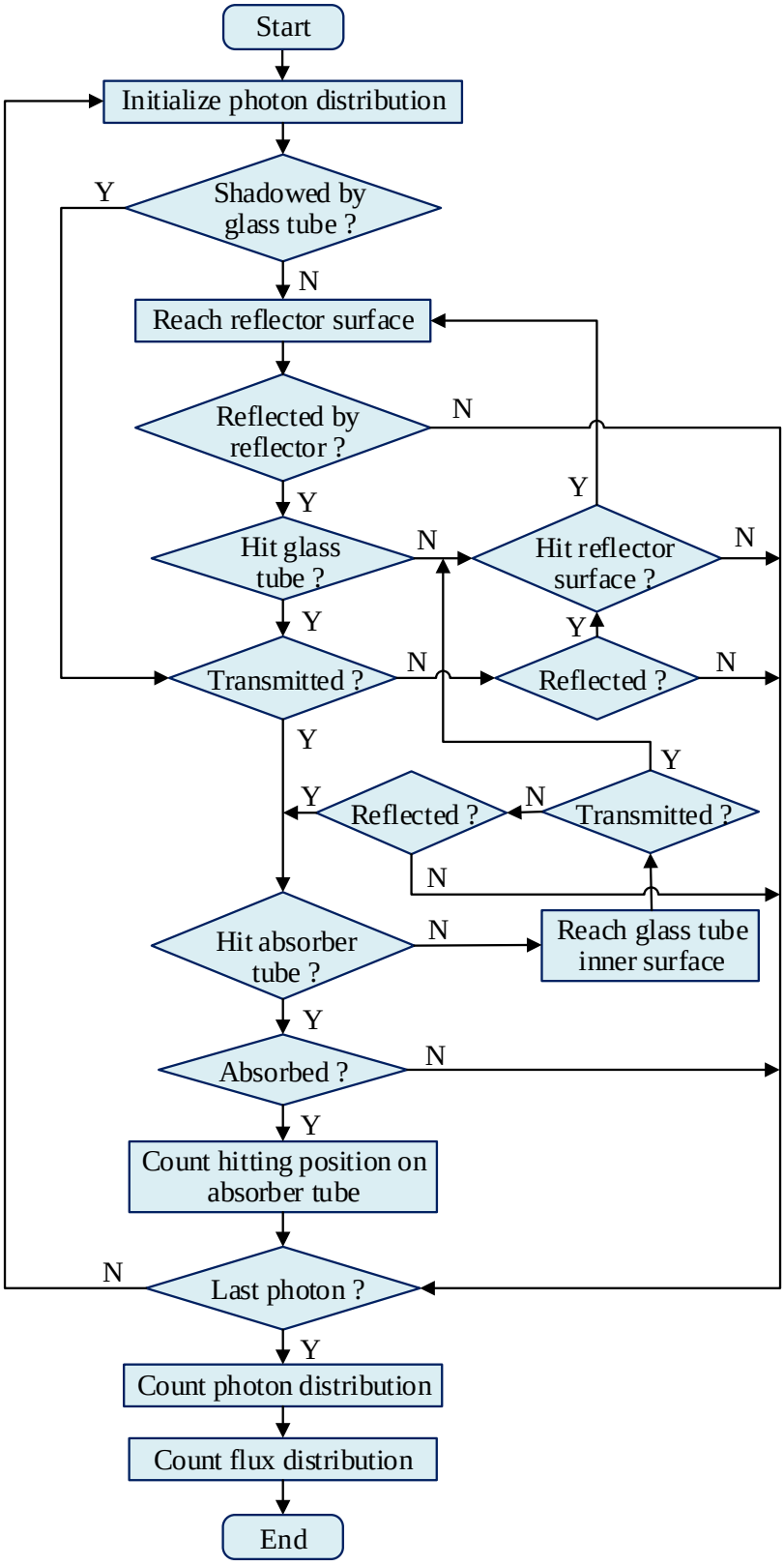

Fig. 5 The flowchart of MCRT

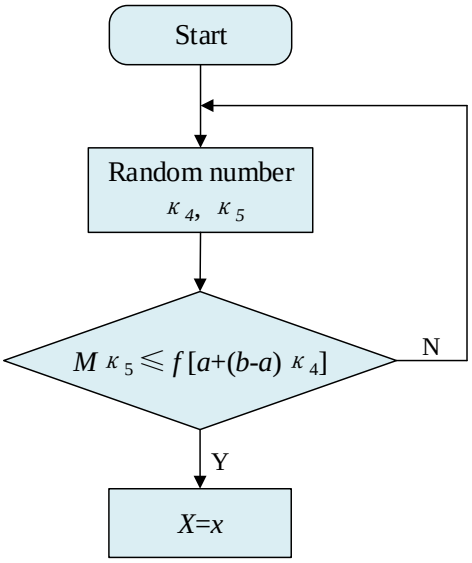

Fig. 6 The flowchart of acceptance-rejection sampling method

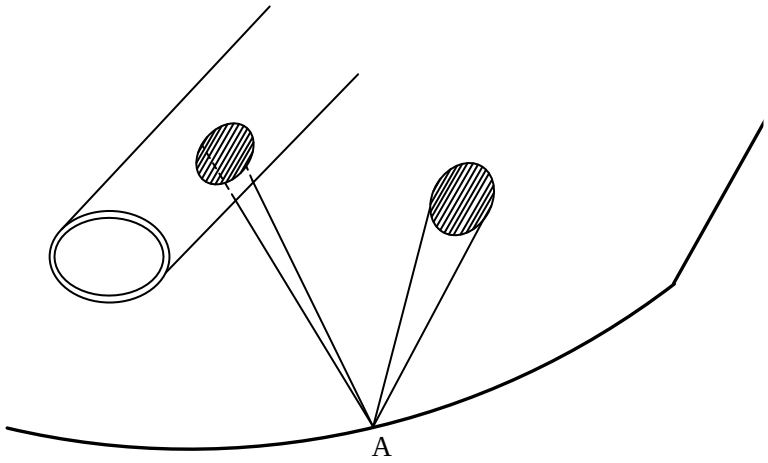

Fig. 7 The reflection process of sun rays

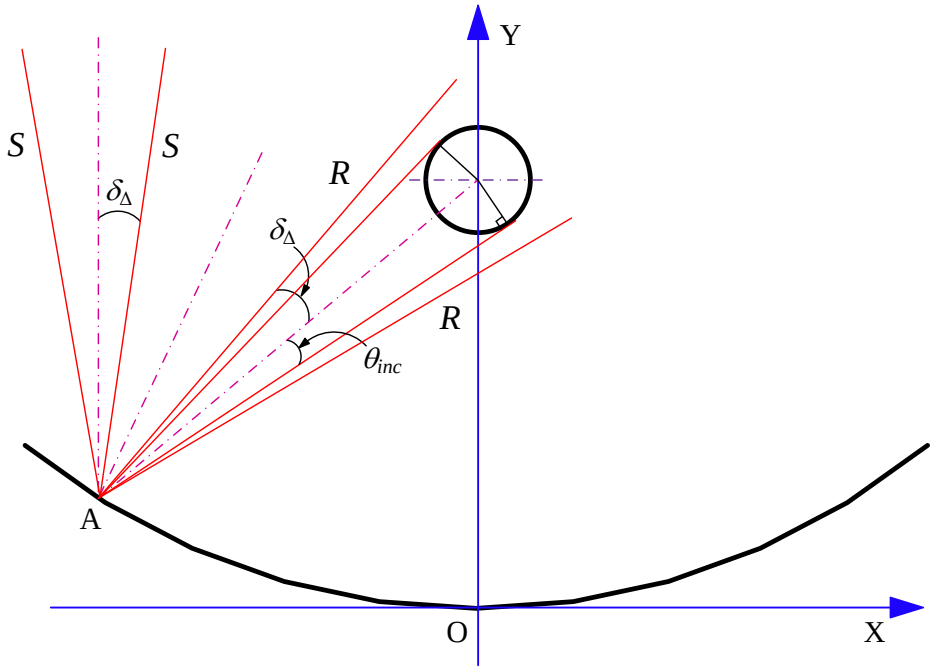

Fig. 8 Reflected rays are intercepted by absorber tube

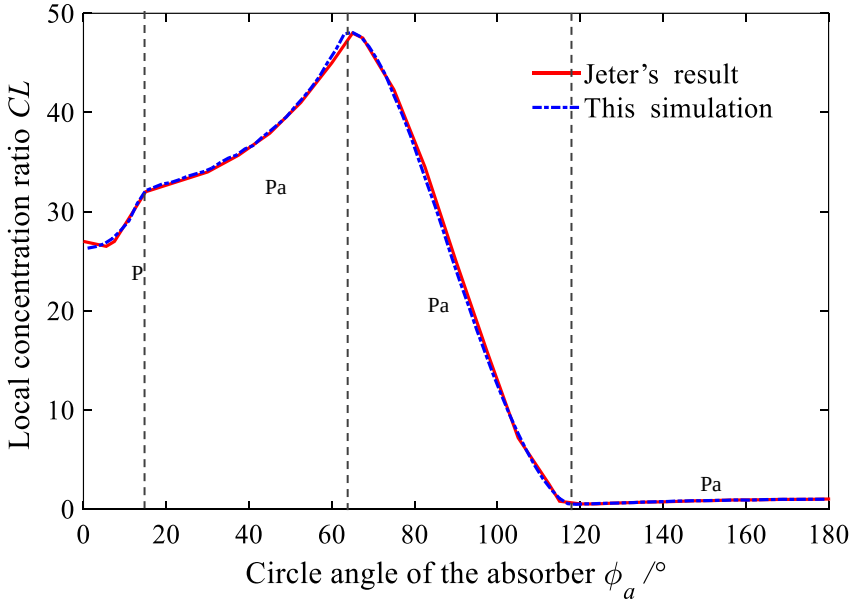

Fig. 9 Comparison of the distribution of the local concentration ratio (*CL*) between this work and Jeter's results

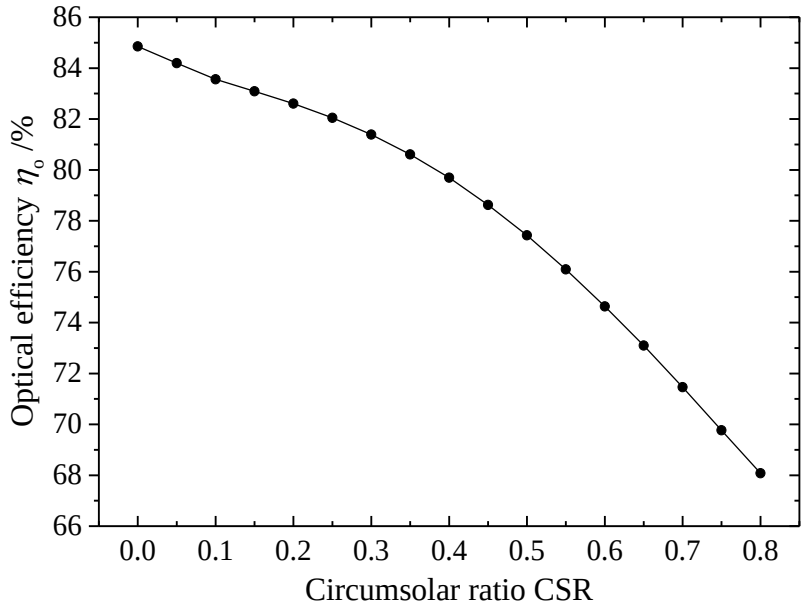

Fig. 10 Effects of circumsolar ratio (CSR) on the optical efficiency (η_o)

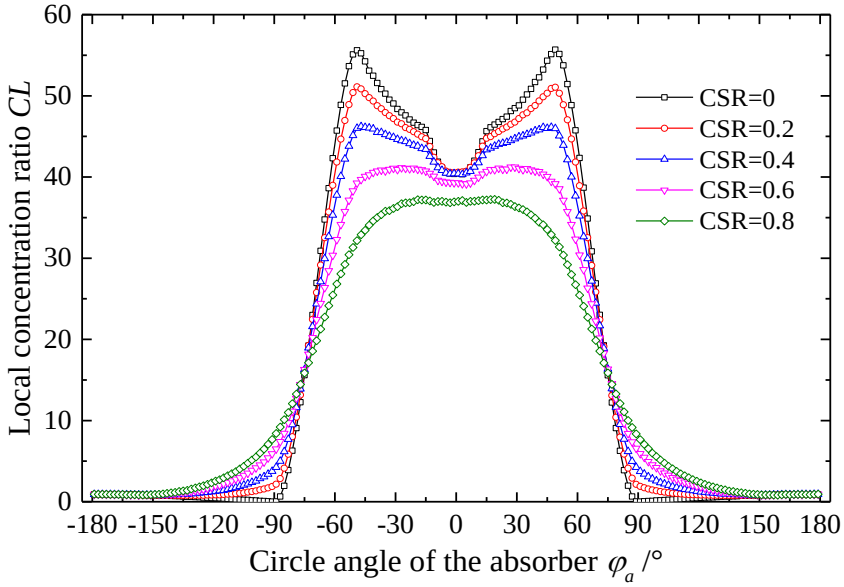

Fig. 11 Effects of circumsolar ratio (CSR) on the distribution of local concentration ratio (*CL*)

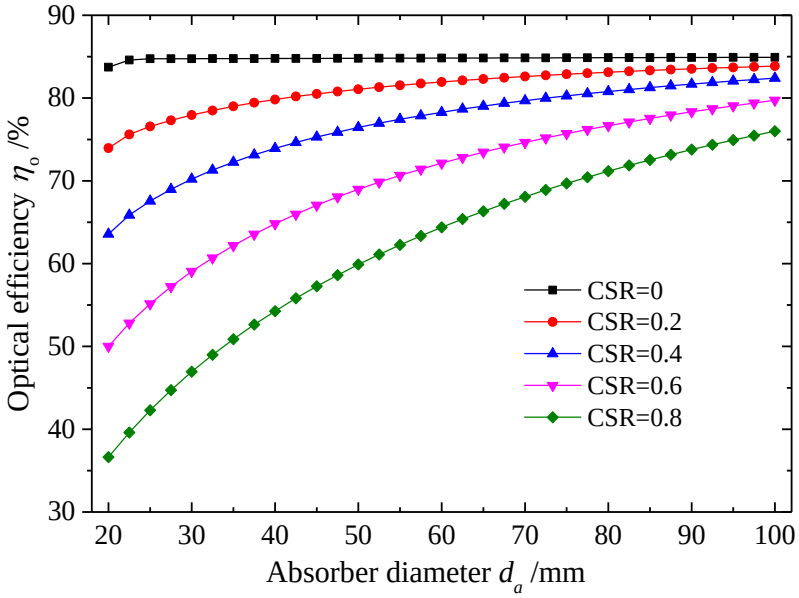

Fig. 12 Variation of optical efficiency (η_o) with absorber diameter (d_a) for different circumsolar ratio (CSR)

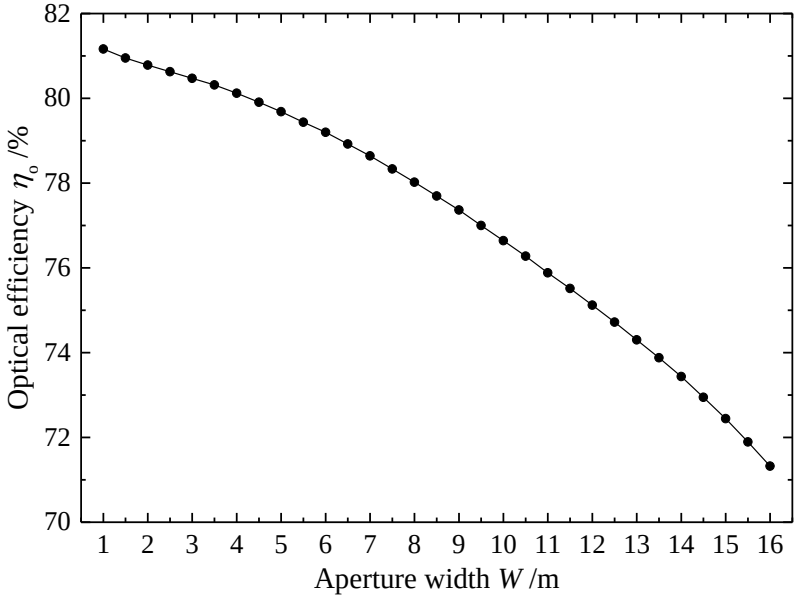

Fig. 13 Variation of optical efficiency (η_o) with aperture width (W) for

CSR=0.4

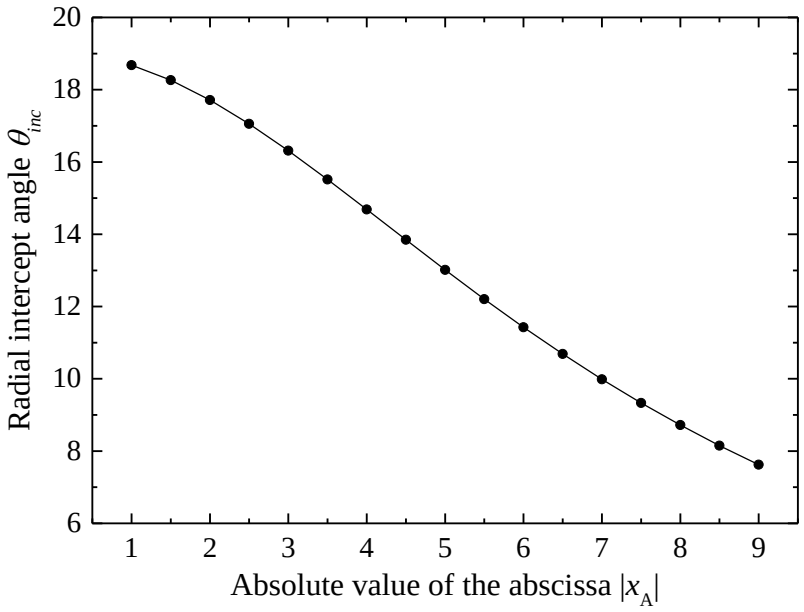

Fig. 14 Variation of radial intercept angle (θ_{inc}) with the absolute value of abscissa of point A ($|x_A|$)

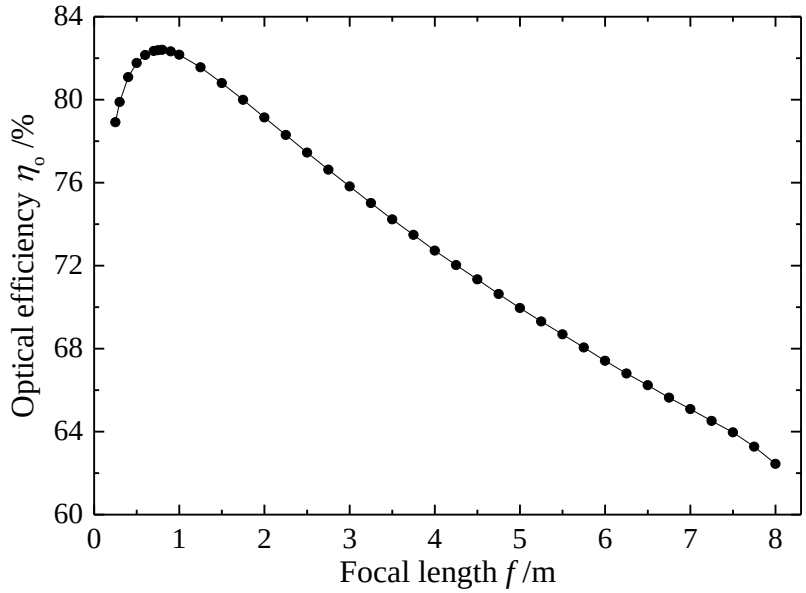

Fig. 15 Variation of optical efficiency (η_o) with focal length (f) for CSR=0.4

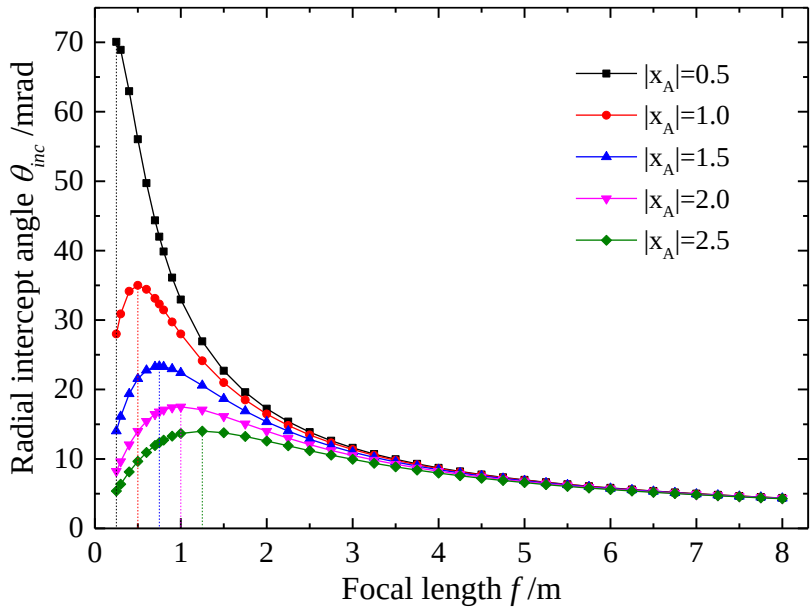

Fig. 16 Variation of radial intercept angle (θ_{inc}) with focal length (f) for different absolute value of abscissa of point A ($|x_A|$)

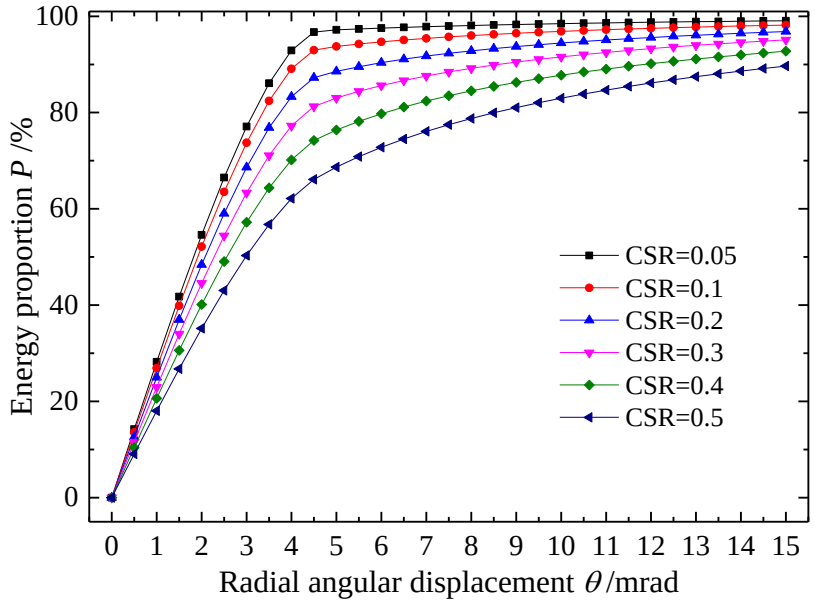

Fig. 17 The proportion of the energy bounded by radial angular displacement (θ) for different CSRs

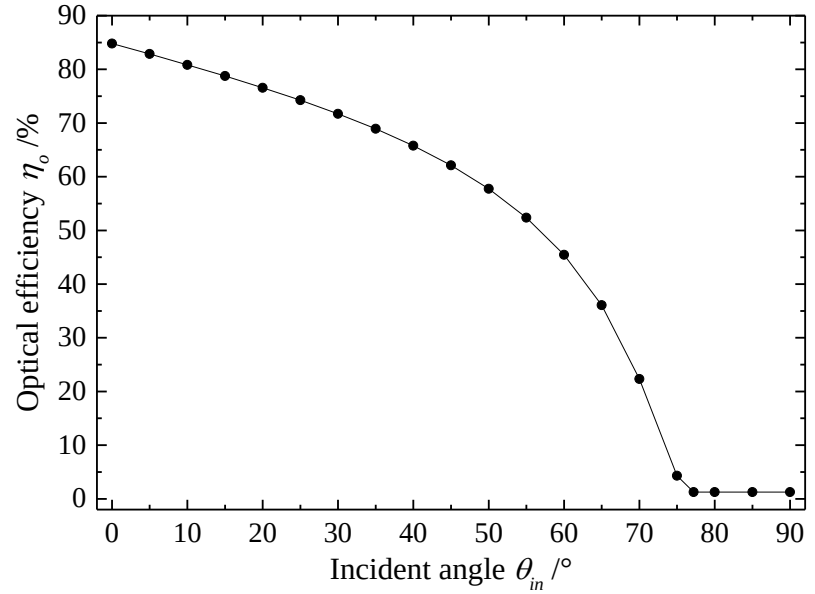

Fig. 18 Effects of incident angle (θ_{in}) on optical efficiency (η_o)

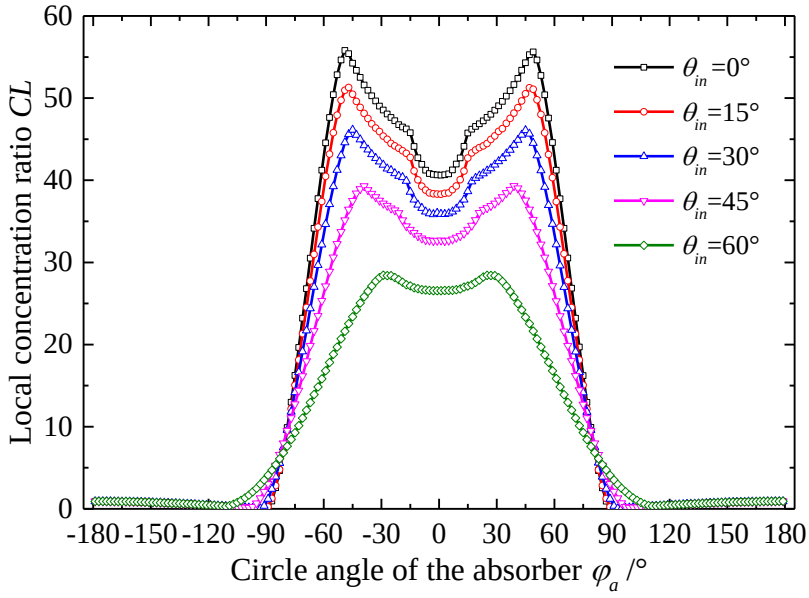

(a) Distribution of local concentration ratio (*CL*) around absorber for different incident angles (θ_{in})

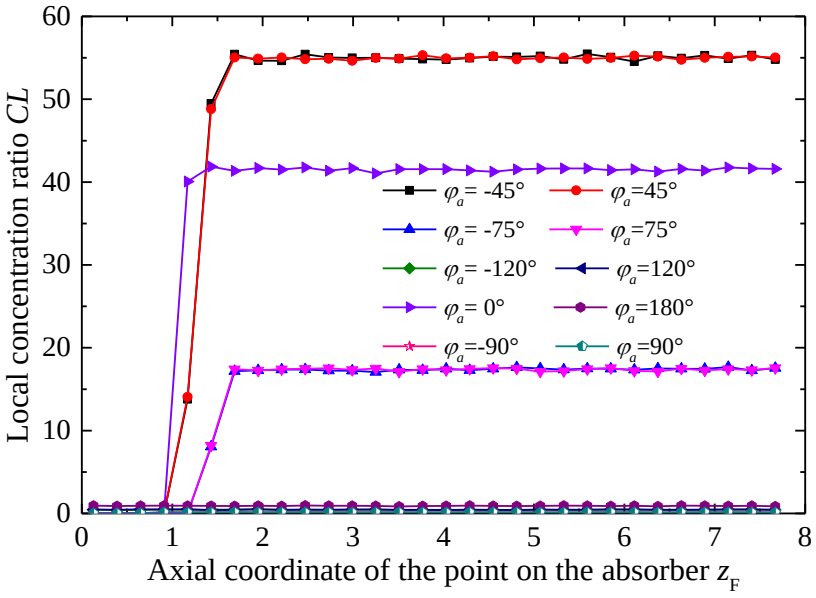

(b) Distribution of local concentration ratio (*CL*) along the absorber for θ_{in}=30°

Fig. 19 Effects of incident angle (θ) on the distribution of local concentration ratio (*CL*)

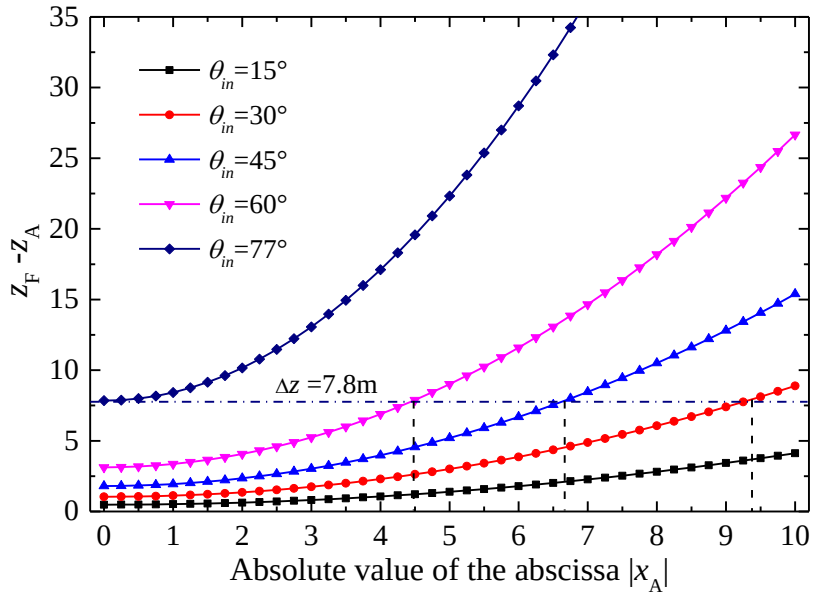

Fig. 20 Variations of $z_F - z_A$ with the absolute value of abscissa of point A ($|x_A|$) for different incident angles (θ_{in})

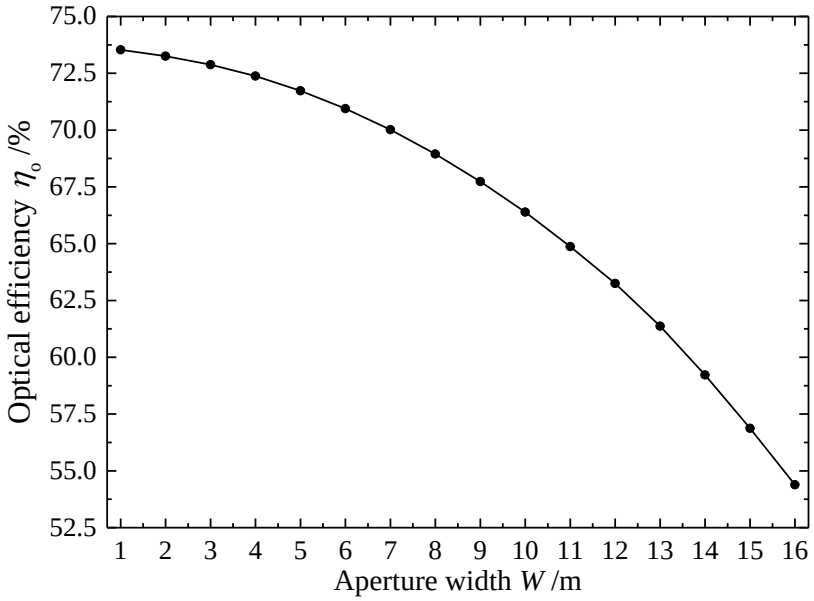

Fig. 21 Effects of aperture width (W) on optical efficiency (η_o) for θ_{in}=30°

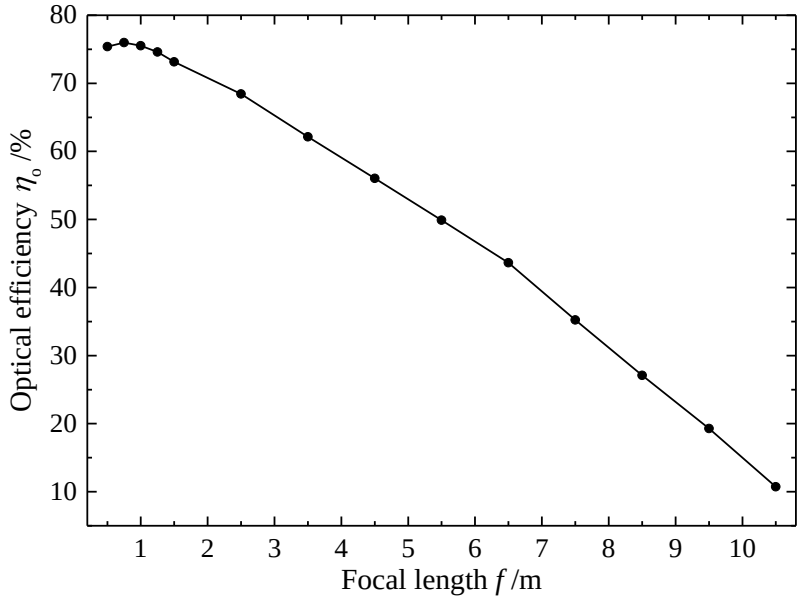

Fig. 22 Effects of focal length (f) on optical efficiency (η_o) for θ_{in}=30°

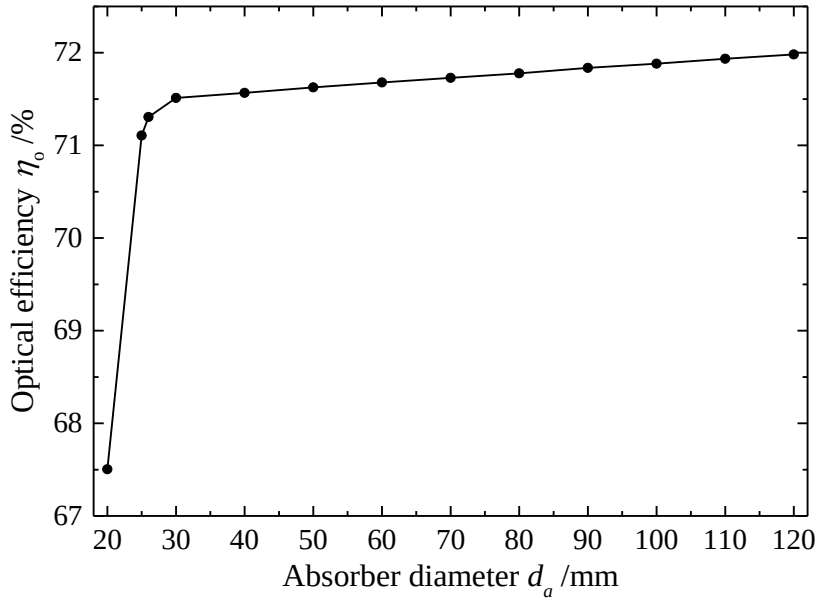

Fig. 23 Effects of absorber diameter (d_a) on optical efficiency (η_o) for θ_{in}=30°

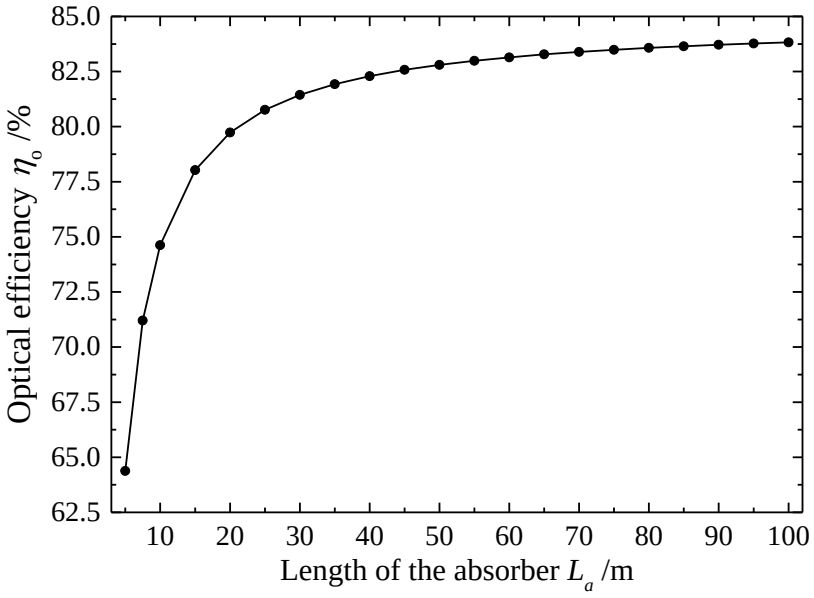

Fig. 24 Effects of absorber length (L_a) on optical efficiency (η_o) for θ_{in} =30°

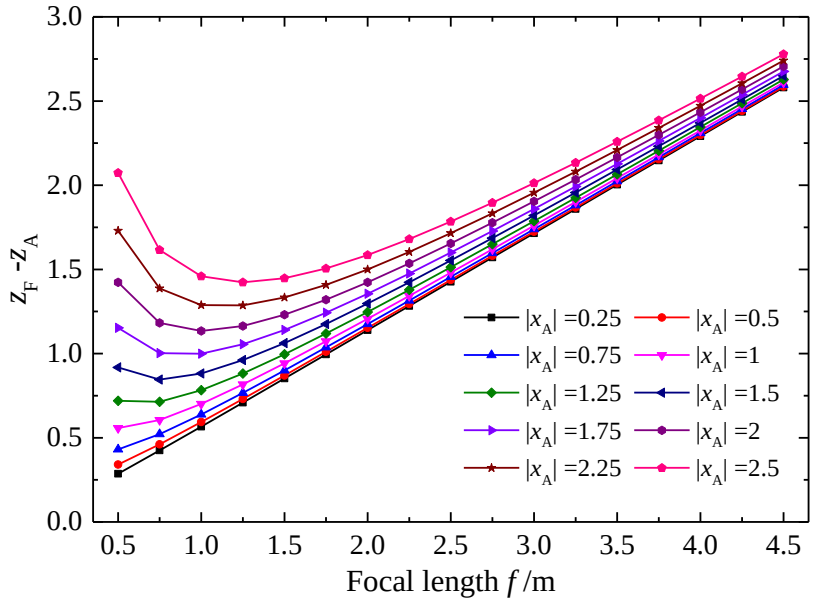

Fig. 25 Variations of $z_F - z_A$ with focal length (f) for different absolute values of the abscissa of point A ($|x_A|$) under condition of θ_{in} =30°

Tables

Table 1 Parameters of SEGS LS-2 PTC module

Parameter	Value	Unit
W	5	m
f	1.84	m
L_a	7.8	m
d_a	0.07	m
d_g	0.115	m
α_a	0.96	——
ρ_r	0.93	——
τ_g	0.95	——